The Sphericity Paradox and the Role of Hoop Stresses in Free Subduction on a Sphere

Stéphanie Chaillat, Gianluca Gerardi, Yida Li, Alexander Chamolly, Zhong-hai Li, Neil M Ribe

The Sphericity Paradox and the Role of Hoop Stresses in Free Subduction on a Sphere

Stéphanie Chaillat[1], Gianluca Gerardi[2,3], Yida Li[3], Alexander Chamolly[4,5], Zhonghai Li[6], Neil M. Ribe[3]

[1]Lab POems, ENSTA-UMA, Palaiseau, France
[2]Centre de Géosciences, Mines ParisTech, Fontainebleau, France
[3]Lab FAST, Université Paris-Saclay, CNRS, F-91405 Orsay, France
[4]Institut Pasteur, Université de Paris, CNRS UMR3738, Developmental and Stem Cell Biology Department, F-75015 Paris, France
[5]Laboratoire de Physique de l'École normale supérieure, ENS, Université PSL, CNRS, Sorbonne Université, Université Paris Cité, F-75005 Paris, France
[6]Key Laboratory of Computational Geodynamics, University of the Chinese Academy of Sciences, Beijing, China

Key Points:

- The dynamical effect of plate sphericity on subduction is greater for smaller plates (the 'sphericity paradox').
- The state of stress in the central portions of subducted slabs is dominated by the longitudinal normal (hoop) stress.
- Mariana slab earthquakes confirm our prediction that convex slab geometry and tensile hoop stress never occur together.

Corresponding author: Neil M. Ribe, `neil.ribe@universite-paris-saclay.fr`

Abstract

Oceanic plates are doubly-curved spherical shells, which influences how they respond to loading during subduction. Here we study a viscous fluid model for gravity-driven subduction of a shell comprising a spherical plate and an attached slab. The shell is 100–1000 times more viscous than the upper mantle. We use the boundary-element method to solve for the flow. Solutions of an axisymmetric model show that the effect of sphericity on the flexure of shells is greater for smaller shells that are more nearly flat (the 'sphericity paradox'). Both axisymmetric and three-dimensional models predict that the deviatoric membrane stress in the slab should be dominated by the longitudinal normal stress (hoop stress), which is typically about twice as large as the downdip stress and of opposite sign. Our models also predict that concave-landward slabs can exhibit both compressive and tensile hoop stress depending on the depth, whereas the hoop stress in convex slabs is always compressive. We test these two predictions against slab shape and earthquake focal mechanism data from the Mariana subduction zone, assuming that the deviatoric stress in our flow models corresponds to that implied by centroid moment tensors. The magnitude of the hoop stress exceeds that of the downdip stress for about half the earthquakes surveyed, partially verifying our first prediction. Our second prediction is supported by the near-absence of earthquakes under tensile hoop stress in the portion of the slab having convex geometry.

Plain Language Summary

Tectonic plates on earth are doubly-curved spherical shells, which influences how they respond to applied forces during subduction. We use axisymmetric and three-dimensional viscous flow models to study the dynamics of spherical shells sinking under gravity into the mantle below. We find the surprising result that the effect of spherical geometry on the bending of shells is greater for smaller shells that are more nearly flat, which we call the 'sphericity paradox'. We also find that the stress in the subducted portions of plates ('slabs') is dominated by the longitudinal normal stress (hoop stress), which is about twice as large as the more familiar downdip stress. Earthquake focal mechanisms from the Mariana subduction zone in the Pacific ocean confirm our prediction that no deep earthquakes should occur under tensile hoop stress in portions of slabs having convex landward geometry.

1 Introduction

An important feature of terrestrial plate tectonics is that plates are doubly-curved spherical shells in their pre-deformed state. The mechanics of such objects is described by the theory of thin shells, which has a long history going back at least to the work of A. E. H. Love (Love, 1944). This theory shows that a doubly-curved shell responds to loads differently than a flat plate. Whereas a flat plate supports a normal load solely by bending stresses, a shell with double curvature does so by bending stresses combined with in-plane 'membrane' stresses (Audoly & Pomeau, 2010). Furthermore, curvature renders a shell stiffer and more resistant to bending, because additional energy has to be expended on stretching in order to change the intrinsic Gaussian curvature (the product of the two principal curvatures) of a surface.

The largest deformations of Earth's tectonic plates occur during subduction. It is therefore natural to focus on subduction when considering how spherical geometry influences the mechanics of terrestrial plates. Naive intuition suggests that the effect of spherical geometry should be minor if the domain of interest has a characteristic lateral dimension much smaller than the earth's radius. It should then be possible to understand the essentials of subduction dynamics using Cartesian models in which the plates are flat in their undeformed state. It is for this reason that the vast majority of numerical subduction models in the literature use two-dimensional (2-D) or three-dimensional (3-D)

Cartesian geometry: representative examples include Ribe (2010), Capitanio and Morra (2012), Cížková and Bina (2013), Garel et al. (2014) and Bessat et al. (2020) in 2-D and Stegman et al. (2010), Li and Ribe (2012), Pusok et al. (2018), Chertova et al. (2018), and Balázs et al. (2021) in 3-D. Gerya (2022) gives a detailed review of numerical models of subduction.

Yet despite the dominance of Cartesian models, the question of how sphericity influences the mechanics of subduction has not been neglected. Early models were purely geometrical (Frank, 1968; Scholz & Page, 1970; Laravie, 1975; Bayly, 1982). Notably, Scholz and Page (1970) and Bayly (1982) proposed that a subducting slab should buckle at depth along the strike of the trench because the space available to it is progressively reduced as it sinks due to the spherical geometry. Schettino and Tassi (2012) used geometrical arguments to determine a relationship between trench curvature, the variation of slab dip and the lateral strain rate, but did not make use of thin-shell theory.

To our knowledge, the first studies to investigate the dynamics of bending spherical shells in a geodynamical context were Tanimoto (1997) and Tanimoto (1998). He solved the equations for a normally loaded spherical elastic shell subject to a buoyancy force proportional to the normal displacement, and showed that the state of stress in the shell is strongly influenced by spherical geometry. Morishige et al. (2010) presented a semi-dynamical model for subduction in a spherical shell, and found that sphericity has only a small effect on the pattern of horizontal flow around slab edges. Mahadevan et al. (2010) investigated the causes of the curvature and segmentation of subduction zones via scaling and numerical analysis of small-amplitude deformation of shallow spherical caps. They found a scaling law for the wavelength of the edge instability ('dimpling') that occurs when a distributed radial body force acts on an elastic shell on an elastic foundation. G. Morra and co-workers used the boundary-element method (BEM) to study large-amplitude subduction of spherical viscous shells, focussing on island arc curvature (Morra et al., 2006), subduction in a mantle with depth-dependent viscosity (Morra et al., 2012), and interaction of several plates (Morra et al., 2012). Chen et al. (2022a) compared the dynamics of subduction in 3-D Cartesian and spherical geometry, and found that the effects of sphericity are important for slabs greater than 2400 km in width. Finally, Chen et al. (2022b) determined a qualitative regime diagram for trench types (shaped like the letters I, C or W) and subduction modes ('vertical folding' and 'weak retreat') in the space of plate age and width. However, none of the aforementioned studies identified the key length scales and dimensionless numbers that control subduction.

Building on the earlier studies cited above, Chamolly and Ribe (2021) used the BEM to investigate subduction of an axisymmetric viscous shell in a mantle with a lower viscosity. This work showed that the role of sphericity is more complicated than it first appears. One would think that the influence of sphericity should be greater for a large shell (e.g. a hemisphere), which is differs more from a plane than a small, shallow shell. This may be called the 'geometrical sphericity' effect. However, there is also a 'dynamical sphericity' effect related to how a spherical shell bends in response to forces applied to its edges. Surprisingly, the trend of this effect is the opposite of the geometrical one: dynamical sphericity is more important for small, nearly flat shells than for large ones. We call this the 'sphericity paradox'. Chamolly and Ribe (2021) used scaling analysis based on thin-shell theory to show that the dynamical sphericity effect is measured by a dimensionless 'dynamical sphericity number' Σ_D proportional to the cotangent of the angle subtended by the plate. This implies that the dynamical effect of sphericity increases as the plate size diminishes.

Our study begins (§ 2.1) by deriving the dynamical sphericity number and determining reference scaling laws for the sinking speed and the longitudinal normal stress ('hoop stress') in a subducting axisymmetric shell. In § 3 we obtain some new results for axisymmetric shells, focusing on the relative magnitudes of the hoop stress and the downdip normal stress in the slab. In § 4, we relax the unrealistic assumption of axisym-

metry and consider 3-D models in which the trench is convex landward. In § 5 we consider the additional effects of radial viscosity stratification, including that associated with an inviscid core. In § 6 we examine the case of a trench that is concave landward, corresponding to a slab with negative Gaussian curvature. In § 7 we test the predictions of our models against observations from the Mariana subduction zone, using the hypothesis that the deviatoric stress in the slab is proportional to the deviatoric part of earthquake centroid moment tensors. Finally, § 8 discusses our results in depth.

2 Physical scalings

The physical fundamentals of subduction of spherical shells can be elucidated by means of scaling analysis of the forces involved. The scalings derived here are hypotheses that we test in subsequent sections.

Figure 1 shows the simplified axisymmetric model that we use for scaling analysis. A shell with thickness h, viscosity η_1 and density $\rho_1 = \rho + \delta\rho_1$ is immersed in a spherical planet with viscosity η_2 and density ρ. The ratio of the viscosities of the shell and the mantle is $\gamma = \eta_1/\eta_2$. The (constant) gravitational acceleration $\mathbf{g}$ is directed radially inward. The planet's outer surface $r = R_0$ is free-slip (vanishing normal velocity and shear traction). The shell consists of a 'plate' $0 \leq \theta \leq \theta_t$ and a 'slab' $\theta_t < \theta \leq \theta_s$. The dip of the slab at its leading end is φ_s. Above the plate is a lubrication or 'sticky air' layer of thickness d, which creates a large normal stress $\sim \delta\rho_1 g h$ that inhibits net downward motion of the plate while allowing it to move freely horizontally and to bulge upward (and of course also downward) due to bending (Ribe, 2010). The radius of the shell's midsurface is

$$r_0(\theta) = \begin{cases} R & (\theta \leq \theta_t) \\ R(1 - b(\zeta^3 - \zeta^4/2)) & (\theta \in [\theta_t, \theta_s]) \end{cases} \tag{1}$$

where $R = R_0 - h/2 - d$ and

$$\zeta = \frac{\theta - \theta_t}{\theta_s - \theta_t}, \quad b = \frac{2(\theta_s - \theta_t)\sin\varphi_s}{2\cos\varphi_s + (\theta_s - \theta_t)\sin\varphi_s}. \tag{2}$$

The functional forms (1) and (2) ensure that the meridional curvature of the midsurface is continuous at the trench and that the dip of the midsurface at $\theta = \theta_s$ is φ_s.

The key length scale in the model is the 'bending length' l_b, the length of the portion of the shell that deforms mainly by bending rather than by extension or shortening. It is the sum of the slab length l and the length of the flexural bulge seaward of the trench, and is indicated schematically in fig. 1. The bending length is diagnostic of the dynamics because the Stokes equations must be solved to determine it. It is not an independent variable because it depends on the geometrical parameters h, d, l, θ_t, θ_s and φ_s and on the viscosity ratio γ. A scaling law for the bending length in 2-D Cartesian geometry is presented in Appendix B of (Ribe, 2010).

The physical scalings discussed below make use of thin-shell theory. The fundamental quantity in this theory is the velocity on the shell's midsurface, with components $\{U, V, W\}$. $U(\theta, \phi)$ is the velocity parallel to the midsurface in the direction of increasing colatitude. $V(\theta, \phi)$ is the component parallel to the midsurface in the direction of increasing longitude, and vanishes if the flow is axisymmetric. The lack of a subscript on V will prevent confusion with the quantities V_{sink}, V_{Stokes}, V_1, V_2 and V_3 introduced later. Finally, $W(\theta, \phi)$ is the velocity normal to the midsurface.

2.1 Geometrical and dynamical sphericity numbers

What we have called the 'geometrical sphericity' of the shell is just the amount by which the shell's midsurface differs from a plane. Geometrical sphericity is small for so-called 'shallow' shells with $\theta_t \ll 1$, and large for e.g. a hemispherical shell with $\theta_t =$

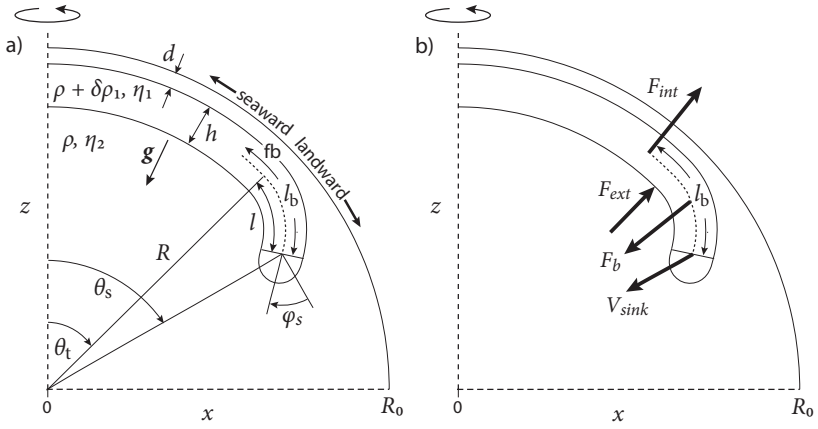

Figure 1. Definition sketch of the axisymmetric model in cross-section (not to scale). (a) A viscous shell with thickness h, viscosity η_1 and density $\rho + \delta\rho_1$ is immersed in a spherical viscous planet with radius R_0, viscosity η_2 and density ρ. The planet's surface $r = R_0$ is free-slip. The shell comprises a spherical 'plate' $\theta \leq \theta_t$ and a 'slab' $\theta_t \leq \theta \leq \theta_s$. The dip of the slab at its leading end is φ_s. The lubrication layer above the plate has thickness d, and the radius of the plate's midsurface is $R = R_0 - h/2 - d$. The gravitational vector $\boldsymbol{g}$ points radially inward. The annotation 'fb' indicates the position of the flexural bulge. (b) Forces acting on the portion of the shell that deforms by bending: the negative buoyancy force F_b, the external traction F_{ext} exerted by the surrounding mantle, and the internal resistance to bending F_{int}. F_{int} is the shear force acting on a vertical plane at the seaward extremity of the bending portion of the shell. Also shown is the radial sinking speed V_{sink} of the tip of the slab.

$\pi/2$. Because the geometrical sphericity increases with θ_t, we may define a 'geometrical sphericity number'

$$\Sigma_G = \theta_t \tag{3}$$

The first step in the derivation of the dynamical sphericity number Σ_D is to identify the forces (per unit length in the longitudinal direction) acting on the bending portion of the plate. Figure 1b shows these. The driving force for subduction is the negative buoyancy F_b acting on the slab. It scales as

$$F_b \sim lhg\delta\rho. \tag{4}$$

The negative buoyancy is balanced by two resisting forces: the external traction F_{ext} applied by the surrounding mantle, and the internal resistance to bending F_{int}. The characteristic stress in the surrounding mantle is $\eta_2 V_{sink}/l_b$, where V_{sink} (>0) is the downward radial velocity of the leading end of the slab. Integrating this over the bending length l_b, we obtain

$$F_{ext} \sim \frac{\eta_2 V_{sink}}{l_b} l_b = \eta_2 V_{sink}. \tag{5}$$

Scaling analysis of the force F_{int} requires the use of thin-shell theory. F_{int} is a viscous reaction force that acts on a cross-section of the shell located at the seaward extremity of the flexural bulge. It is equal to the integral across the shell (the 'resultant') of the midsurface-perpendicular shear stress $\sigma_{\theta z}$ acting on the cross-section. Its explicit definition is (Novozhilov, 1959)

$$F_{int} = \int_{-h/2}^{h/2} \sigma_{\theta z}(1 - K_\phi z)\mathrm{d}z \equiv N_\theta \tag{6}$$

where z is a coordinate perpendicular to the midsurface $z = 0$ and K_ϕ is the longitudinal curvature of the midsurface. If the flow is axisymmetric, N_θ is related to the colatitudinal bending moment M_θ and the longitudinal bending moment M_ϕ by (Novozhilov, 1959, eqn. (7.8))

$$N_\theta = \frac{1}{A_\theta A_\phi}\left[\partial_\theta(A_\phi M_\theta) - M_\phi \partial_\theta A_\phi\right] \tag{7}$$

where

$$A_\theta = \left[r_0^2 + (\partial_\theta r_0)^2\right]^{1/2}, \quad A_\phi = r_0 \sin\theta \tag{8}$$

are the Lamé parameters of the shell's midsurface. A_θ is the ratio of a change $\mathrm{d}s$ of arclength along the shell's midsurface to the associated change of colatitude $\mathrm{d}\theta$, and A_ϕ is defined similarly for changes in ϕ. Later we shall also need the two principal curvatures of the midsurface, defined as

$$K_\theta = -\frac{r_0^2 + 2(\partial_\theta r_0)^2 - r_0 \partial^2_{\theta\theta} r_0}{(r_0^2 + (\partial_\theta r_0)^2)^{3/2}}, \quad K_\phi = \frac{\partial_\theta r_0 \cot\theta - r_0}{r_0 (r_0^2 + (\partial_\theta r_0)^2)^{1/2}}. \tag{9}$$

K_θ and K_ϕ are positive if the center of curvature lies on the side of the midsurface in the direction of the outward-pointing normal vector. Therefore both curvatures are negative for a spherical shell. The constitutive relations for the bending moments are

$$M_\theta = \frac{\eta_1 h^3}{3}\left(\dot\kappa_\theta + \frac{1}{2}\dot\kappa_\phi\right), \quad M_\phi = \frac{\eta_1 h^3}{3}\left(\dot\kappa_\phi + \frac{1}{2}\dot\kappa_\theta\right) \tag{10}$$

where

$$\dot\kappa_\theta = -\frac{1}{A_1}\partial_\theta\left(\frac{1}{A_\theta}\partial_\theta W + K_\theta U\right), \quad \dot\kappa_\phi = -\frac{1}{A_\theta A_\phi}\partial_\theta A_\phi\left(\frac{1}{A_\theta}\partial_\theta W + K_\theta U\right) \tag{11}$$

are bending rates of the shell's midsurface in the colatitudinal and longitudinal directions, respectively.

For scaling purposes, we set $A_\theta \approx R$ and $A_\phi \approx R\sin\theta$, the Lamé parameters for a spherical surface of radius R. Retaining only the dominant terms (the first terms in the parentheses) in (11), we have

$$\dot{\kappa}_\theta \sim -\frac{1}{R^2}\partial^2_{\theta\theta}W, \quad \dot{\kappa}_\phi \sim -\frac{\cot\theta}{R^2}\partial_\theta W. \tag{12}$$

Furthermore, (7) takes the form

$$N_\theta \approx \frac{1}{R}(M_\theta - M_\phi)\cot\theta + \frac{1}{R}\partial_\theta M_\theta. \tag{13}$$

Now the length scale for colatitudinal derivatives is the bending length l_b, which implies $\partial_\theta \sim R/l_b$. Moreover, $W \sim V_{sink}$. Combining these scalings with (10) and (12) we obtain

$$M_\theta, M_\phi \sim \frac{\eta_1 h^3 V_{sink}}{l_b^2}\max\left(1, \frac{l_b\cot\theta}{R}\right), \tag{14}$$

Upon choosing θ_t as a representative value of θ and replacing R by the earth's radius R_0, the second term in brackets in (14) becomes the dynamical sphericity number

$$\Sigma_D = \frac{l_b}{R_0}\cot\theta_t. \tag{15}$$

The dimensionless number Σ_D measures the effect of sphericity on the flexural response of the shell to loading. A greater Σ_D means a larger bending moment (and hence a larger force F_{int} resisting subduction) for a given V_{sink}.

The 'flat-earth' limit $\Sigma_D \to 0$ can be obtained in two ways. The first is to set $\theta_t = \pi/2$. This implies the surprising result that a hemispherical shell should bend under a load in a way similar to a flat plate. The second way to obtain $\Sigma_D \to 0$ is to write

$$\Sigma_D = \frac{l_b}{L}\epsilon\cot\epsilon \quad \text{where} \quad \epsilon = \frac{L}{R_0} \tag{16}$$

and $L = R_0\theta_t$ is the length of the plate measured along the earth's surface. Because $\epsilon\cot\epsilon \leq 1$, we obtain $\Sigma_D \to 0$ when $l_b/L \to 0$. The dynamical sphericity therefore vanishes when the bending length is much smaller than the plate length. The bending portion of the shell then no longer 'feels' the plate's curvature.

The definition (15) of Σ_D implies the seemingly paradoxical result that dynamical sphericity is greater for a small shell than for a large one. An intuitive understanding of this can be obtained by cutting two shells from a basketball: a large one equal to a full hemisphere, and a small one in the form of a shallow spherical cap. Now balance each shell upside down on the point of an upright pencil, and deform them slightly by applying radially directed forces to opposite sides. You will find that a given applied force produces a smaller deformation of the shallow cap than of the hemisphere: the latter is 'floppy' whereas the former is 'stiff'. The same applies to viscous shells if 'deformation' is replaced by 'rate of deformation'.

2.2 Sinking speed

A useful diagnostic parameter for subduction models is the sinking speed $V_{sink} > 0$ of the slab's leading edge. It is controlled by the balance of the three forces F_b, F_{ext} and F_{int} shown in fig. 1b. The balance $F_b \sim F_{ext}$ implies a characteristic Stokes velocity scale

$$V_{Stokes} = \frac{lhg\delta\rho_1}{\eta_2} \tag{17}$$

Now the normalized sinking speed V_{sink}/V_{Stokes} must be a function of the ratio F_{int}/F_{ext}. Using (5), (13) and (14), we find

$$F_{int} \sim \eta_2 V_{sink} f_1(St, \Sigma_D) \tag{18}$$

where

$$St = \frac{\eta_1}{\eta_2}\left(\frac{h}{l_b}\right)^3 \tag{19}$$

is a dimensionless 'flexural stiffness' and f_1 is an unknown function. St determines whether subduction of the shell is resisted primarily by externally applied tractions ($St \leq 1$) or by its internal resistance to bending ($St \gg 1$). The same parameter is relevant for initially flat plates in 2-D and 3-D Cartesian geometry (Ribe, 2010; Li & Ribe, 2012). The requirement that V_{sink}/V_{Stokes} be a function of F_{int}/F_{ext} now takes the form (Chamolly & Ribe, 2021)

$$\frac{V_{sink}}{V_{Stokes}} = f_2(St, \Sigma_D, \Sigma_G, \varphi_s) \tag{20}$$

where f_2 is an unknown function. The last two purely geometrical arguments of f_2 account for the effects of geometrical sphericity and of a variable dip angle, neither of which can be determined by scaling analysis.

2.3 Membrane stresses

We now turn to the so-called 'membrane' stresses in the shell: the downdip normal stress $\sigma_{\theta\theta}$ and the longitudinal normal stress $\sigma_{\phi\phi}$ ('hoop stress'). These are associated with in-plane extension or shortening (membrane deformation) and are constant across the shell, whereas the normal stresses associated with bending vary linearly across the shell. Membrane stresses are usually measured in terms of their resultants

$$T_\theta = \int_{-h/2}^{h/2} \sigma_{\theta\theta}(1 - K_\phi z)\mathrm{d}z = 4\eta_1 h\left(\dot\epsilon_\theta + \frac{1}{2}\dot\epsilon_\phi\right), \tag{21a}$$

$$T_\phi = \int_{-h/2}^{h/2} \sigma_{\phi\phi}(1 - K_\theta z)\mathrm{d}z = 4\eta_1 h\left(\dot\epsilon_\phi + \frac{1}{2}\dot\epsilon_\theta\right), \tag{21b}$$

where

$$\dot\epsilon_\theta = \frac{1}{A_\theta}\partial_\theta U - K_\theta W, \quad \dot\epsilon_\phi = \frac{1}{A_\theta A_\phi}(\partial_\theta A_\phi)U - K_\phi W \tag{22}$$

are the rates of extension or shortening of the midsurface in the θ- and ϕ- directions, respectively. The expressions (22) are valid for axisymmetric shells. Because earthquakes respond to deviatoric stress rather than total stress, we introduce two additional resultants of the deviatoric downdip and hoop stress:

$$D_\theta = 2\eta_1 h\dot\epsilon_\theta \equiv \frac{2T_\theta - T_\phi}{3}, \quad D_\phi = 2\eta_1 h\dot\epsilon_\phi \equiv \frac{2T_\phi - T_\theta}{3}. \tag{23}$$

We now perform a scaling analysis of the hoop stress resultant T_ϕ. The dominant contribution to T_ϕ is the strain rate $\dot\epsilon_\phi$, whose magnitude can be estimated as

$$\dot\epsilon_\phi \sim -K_\phi W. \tag{24}$$

Using the expression (1) for $r_0(\theta)$ to evaluate K_ϕ at $\theta = \theta_s$ assuming $\varphi_s = 45^\circ$ and $\theta_s - \theta_t \ll 1$, we find

$$K_\phi(\theta_s) = -\frac{(2 + \theta_s - \theta_t)(1 + \cot\theta_s)}{2\sqrt{2}R} \sim -R^{-1}\max(1, \cot\theta_s). \tag{25}$$

Combining (25) with (21b) and setting $R \approx R_0$, we find

$$T_\phi \sim \frac{\eta_1 h}{R_0} W_s \max(1, \cot\theta_s) \tag{26}$$

where $W_s = W(\theta_s)$.

Table 1. Parameters of the reference model

R_0/h	d/h	θ_t	$\theta_s - \theta_t$	φ_s	γ
63.7	0.3	30°	5°	45°	316

3 New results for axisymmetric subduction

In this section we present new axisymmetric numerical solutions that extend those of Chamolly and Ribe (2021). Unless otherwise stated, the models discussed here and subsequently have the reference dimensionless parameters given in Table 1. For simplicity, we suppose that there is no inviscid core and that the mantle is isoviscous. These unrealistic assumptions will be relaxed later.

The flow in the shell and in the surrounding mantle satisfies the Stokes equations of slow incompressible viscous flow. Because inertia is negligible in planetary mantles, the temporal history of a subducting shell is just a sequence of quasi-static configurations. The essential dynamics of subduction can therefore be understood by means of instantaneous solutions of the Stokes equations, to which we limit ourselves in this study.

We solve the Stokes equations using the boundary-element method (BEM) of Chamolly and Ribe (2021). The BEM calculates the vector velocity at all nodes on the discretized interface between the shell and the surrounding mantle. As far as the method is concerned, the interface can have any shape. However, in our case the interface is the surface of a thin shell with one short dimension and two long ones. We can therefore use the theory of thin viscous shells to interpret our BEM solutions. As noted in § 2, thin-shell theory is expressed in terms of the midsurface velocity with components U, V and W. The most accurate way to determine the midsurface velocity from a BEM solution is to exploit a prediction of thin-shell theory according to which all components of the velocity vary at most linearly across the shell to lowest order. The midsurface velocity is therefore a simple average of the velocities at the two points where the normal to the midsurface pierces the interface. In the axisymmetric model studied in the present section $V = 0$ while U and W are independent of ϕ. In the three-dimensional models to be examined later, $V \neq 0$ and U, V and W are all functions of both θ and ϕ. The kinematical quantities $\dot{\kappa}_\theta$, $\dot{\kappa}_\phi$, $\dot{\epsilon}_\theta$ and $\dot{\epsilon}_\phi$ introduced in § 2 are obtained from the midsurface velocity field by differentiation.

3.1 Illustrative kinematical and dynamical fields

Figures 2a–d show several kinematical and dynamical quantities of interest as a function of arclength along the midsurface of a shell with the parameters of Table 1. Fig. 2a shows the vector velocity field, which corresponds to subduction by trench rollback. Fig. 2b shows the radial velocity u_r versus arclength s along the midsurface. The label 'fb' indicates an interval of upward radial velocity, corresponding to flexural bulging. Fig. 2c shows the bending rate $\dot{B}_\theta = -\dot{\kappa}_\theta - \dot{\kappa}_\phi/2$, which is nonzero in a boundary layer whose arcwise extent is just the bending length l_b. Our definition of l_b is indicated. Finally, fig. 2d shows the rates of viscous dissipation as functions of arclength associated with flexural (red) and membrane (blue) deformation. Dissipation in the shallower portion of the slab is dominated by flexure, and in the deeper portion by membrane deformation. Dissipation in the plate ($s/R_0 < 0.4$) is dominated by shortening. The local minima of the red curve correspond to points of inflexion where the bending rate changes sign.

We now examine two quantities of special interest for the dynamics of axisymmetric shells: the sinking speed V_{sink} and the hoop stress resultant.

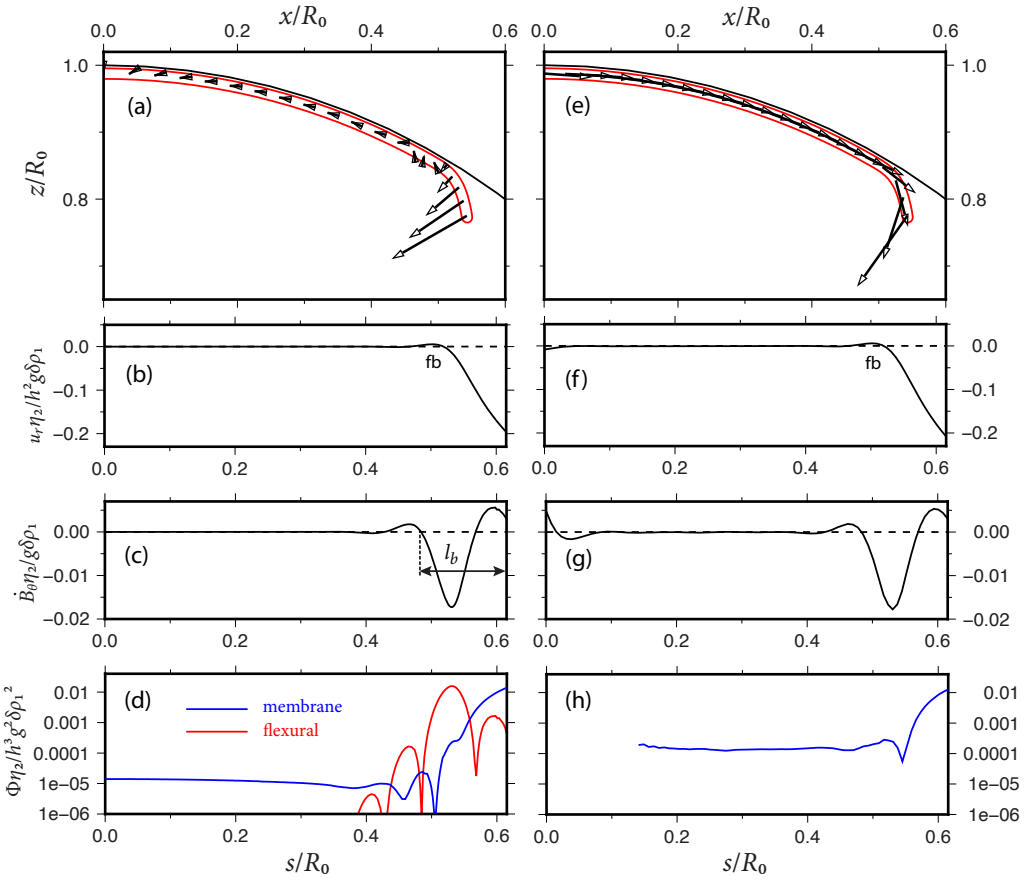

Figure 2. Instantaneous kinematical fields on the midsurface of shells with the reference parameters of Table 1. Parts (a)–(d) are for an axisymmetric shell, and parts (e)–(h) are for the mirror plane $\phi = 0$ of a three-dimensional shell with $\phi_f = \pi/2$. (a) and (d): vector velocity; (b) and (f): radial velocity u_r; (c) and (g): bending rate $\dot{B}_\theta$; (d) and (h): rates of viscous dissipation due to flexural (red) and membrane (blue) deformation. The labels 'fb' in parts (b) and (f) indicate flexural bulging.. The definition of the bending length l_b is shown in part (c). For reasons explained in the text, the membrane dissipation rate for $s/R_0 < 0.14$ and the flexural dissipation rate are not shown in part (h).

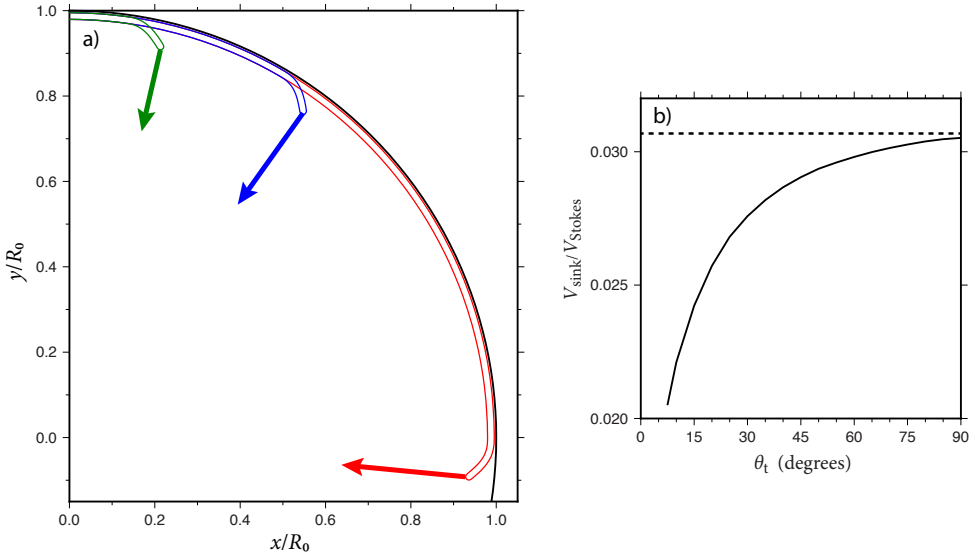

Figure 3. Sinking speed V_{sink} of a slab as a function of the plate size θ_t, for a shell with the standard parameters of Table 1 except $\theta_s - \theta_t = 5.5°$ and $\gamma = 560$. (a) V_{sink}, indicated by the lengths of the arrows, for three shells with $\theta_t = 7.5°$ (green), 30° (blue), and 90° (red). (b) Normalized sinking speed V_{sink}/V_{Stokes} vs. θ_t. The horizontal dashed line indicates the sinking speed of a 2-D slab with the same length and dip as in the 3-D case.

3.2 Sinking speed V_{sink}

Here we test two predictions of our scaling analysis of V_{sink}. The first is that V_{sink} should decrease as the plate size θ_t decreases, because the greater dynamical sphericity of small plates makes them stiffer. The second is that a hemispherical shell should bend under edge loading in a way identical to a flat plate.

Figure 3 shows the slab sinking speed V_{sink} as a function of θ_t for a shell having the reference parameters of Table 1 except for $\theta_s - \theta_t = 5.5°$ and $\gamma = 560$. In figure 3a, the lengths of the arrows indicate V_{sink} for three shells with $\theta_t = 7.5°$ (green), 30° (blue), and 90° (red). As predicted by the scaling analysis, V_{sink} decreases as θ_t decreases, by 33% from $\theta_t = 90°$ (a hemispherical shell) to $\theta_t = 7.5°$. Fig. 3b shows the normalized sinking speed V_{sink}/V_{Stokes} as a function of θ_t, together with the value (horizontal dashed line) predicted by an independent 2-D Cartesian BEM code with an initially flat plate (Ribe, 2010) for the same values of γ, d/h, φ_s, and the slab length. The 2-D BEM prediction is within 1% of the axisymmetric BEM prediction for $\theta_t = 90°$, demonstrating that a hemispherical shell subducts like a flat plate. Figure 3 was constructed assuming a fixed slab length, and therefore a fixed V_{Stokes}. The rapid decrease of V_{sink}/V_{Stokes} for small θ_t is therefore due to the decrease of V_{sink} as the plate size decreases.

3.3 Hoop stress resultant

We now turn our attention to the hoop stress in the shell. This stress component is important because it can drive longitudinal buckling instabilities when it is compressive (Ribe et al., 2007). Furthermore, in § 7 we show that the hoop stress is a major determinant of earthquake focal mechanisms in deep slabs.

Figure 4 shows the normalized maximum hoop stress resultant $R_0|T_\phi|_{max}/\eta_1 h|W_s|$ for 175 BEM solutions with different values of $\theta_s - \theta_t$ and the viscosity ratio γ. The points collapse onto a universal curve that is well fit by $3.161 + 1.306\cot\theta_s$ (black line). This validates our proposed scaling law (26) to within additive and multiplicative constants of order unity, which scaling analysis is in principle unable to determine. Note that the quantity $|W_s|$ in the scaling law is not an independent variable, but itself obeys a scaling law similar to the one (20) for V_{sink}. What fig. 4 shows is that the scaled hoop stress resultant is entirely controlled by θ_s and the velocity W_s normal to the midsurface.

A useful way to measure the effect of dynamical sphericity on the hoop stress is to compare $|T_\phi|_{max}$ for a given θ_s with its value for $\theta_s = 90°$. Figure 4 shows that this ratio is 2.0 for $\theta_s = 25.5°$ and 2.8 for $\theta_s = 13.5°$. Dynamical sphericity thus increases the hoop stress by a factor of 2–3 for small plates relative to a hemispherical plate. In comparison, the dynamical sphericity effect on the sinking speed V_{sink} is only 20–33% for small plates (figure 3).

Next we examine the total stress resultants $T_\phi(s)$ and $T_\theta(s)$ and the deviatoric stress resultants $D_\phi(s)$ and $D_\theta(s)$ as functions of arclength along the midsurface. Figure 5 shows the resultants for shells with $\theta_t = 30°$ (fig. 5b) and $\theta_t = 60°$ (fig. 5c). The shape of the shell for $\theta_t = 30°$ is shown in fig. 5a. Surprisingly, in both cases the state of stress in most of the slab is dominated by the compressive hoop stress. Focusing on the deviatoric stress resultants, we see that $D_\phi \approx -2D_\theta$ for both values of θ_t.

Our axisymmetric model, despite its idealized character, has uncovered three surprising aspects of free subduction of spherical shells. The first is the sphericity paradox: the fact that the effect of sphericity on the flexure of shells is greater when the shell is smaller and more nearly flat. The second is that a hemispherical shell loaded along its edge should bend like a flat plate. The third is that the state of deviatoric stress in a subducting slab — at least one that is convex landward — should be dominated by the hoop stress rather than the downdip stress. We can now use these results as guides as we turn to examine more realistic 3-D models.

4 Three-dimensional model with a convex-landward trench

Figure 6 sketches the geometry of the first 3-D model we shall examine. The shell is a segment of a spherical cap, bounded by half a small circle $\theta = \theta_t$ (the trench) and a portion of a meridian $\phi = \phi_f$, where ϕ is the longitude. Fig. 6b shows a cross-section of the model along a meridian. The model comprises three fluid volumes: a shell V_1 (viscosity η_1), an upper mantle V_2 (viscosity η_2) and a lower mantle V_3 (viscosity η_3) bounded below by an inviscid core. The two independent viscosity ratios are $\gamma = \eta_1/\eta_2$ and $\lambda = \eta_3/\eta_2$.

The only boundary condition applied to the model is that $\phi = 0$ is a plane of mirror symmetry, which allows us to reduce the size of the problem domain by a factor of two. The matching conditions on velocity and stress at the various fluid-fluid interfaces have already been imposed during the derivation of the boundary-integral equations. Finally, the free-slip boundary conditions at the surface $r = R_0$ are satisfied automatically by the Green's functions we use.

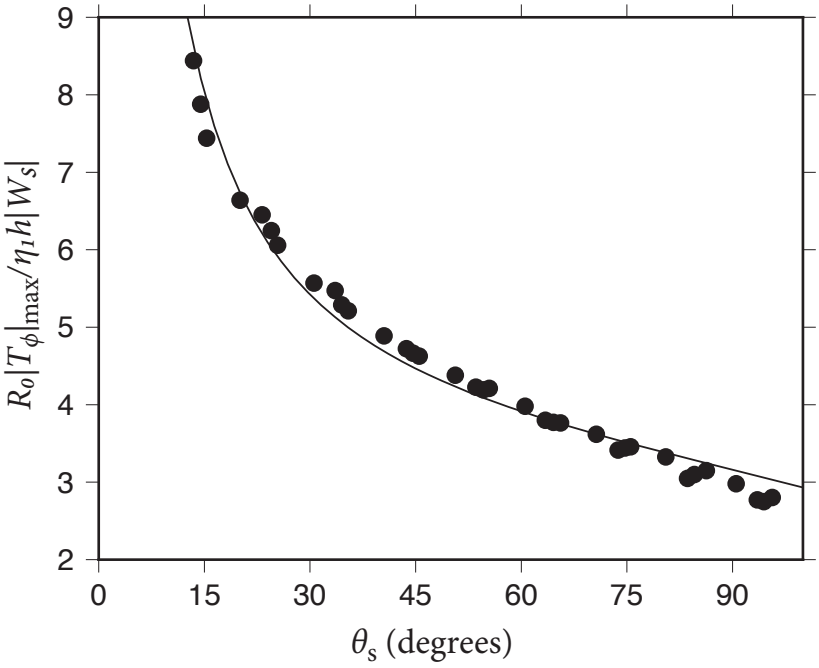

Figure 4. Normalized maximum hoop stress resultant T_ϕ predicted by the axisymmetric BEM model as a function of θ_s. The results of 175 BEM solutions for $\theta_s - \theta_t \in [4^\circ, 7.5^\circ]$ and $\gamma \in [100, 1000]$ are shown. Other model parameters are as in Table 1. Each circle represents the average of five solutions with different values of γ. The black line is $3.161 + 1.306 \cot \theta_s$.

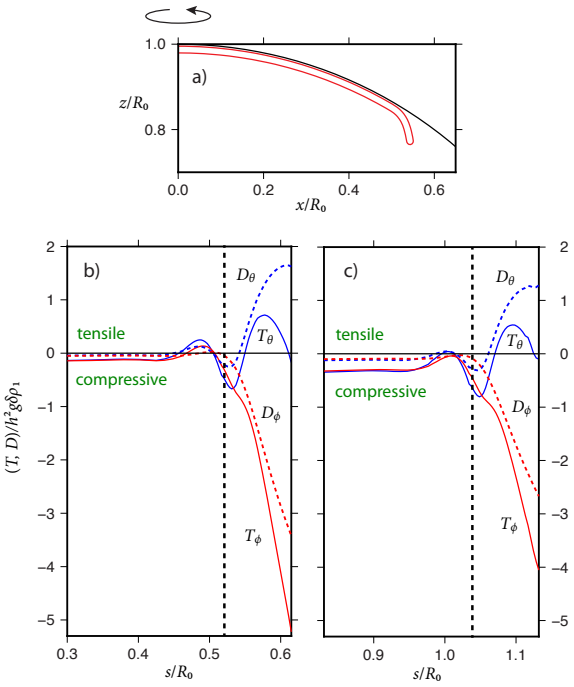

Figure 5. Comparison of the total stress resultants $T_\phi(s)$ and $T_\theta(s)$ and the deviatoric stress resultants $D_\phi(s)$ and $D_\theta(s)$ for axisymmetric shells as functions of arclength s along the mid-surface. (a) Cross-section of the shell for $\theta_t = 30°$. Values of other model parameters are those of Table 1. (b) Stress resultants for the shell shown in part (a). The black vertical dashed line shows the position of the trench. (c) Same as (b), except for $\theta_t = 60°$.

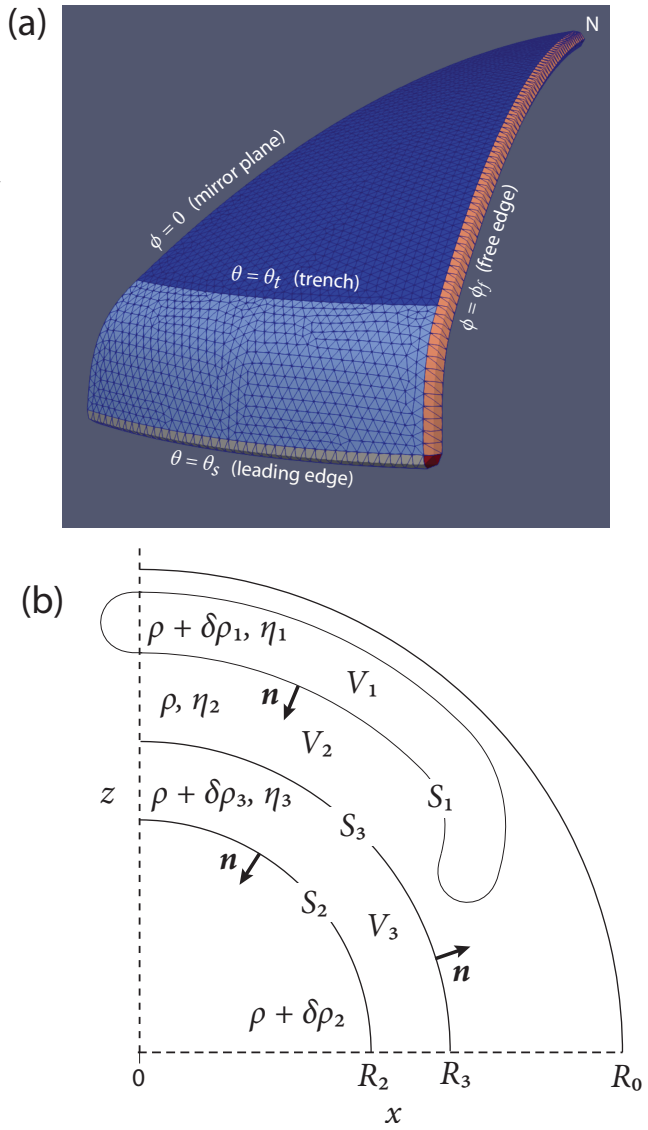

Figure 6. (a) Bird's-eye view of the three-dimensional model with a convex-landward trench. The plate is a segment of a spherical cap, bounded by a trench $\theta = \theta_t$ and a free edge $\phi = \phi_f$, where ϕ is the longitude. The symbol N at upper right indicates the north pole of the spherical coordinate system. The meridian $\phi = 0$ is a plane of mirror symmetry. The slab $\theta_t \leq \theta \leq \theta_s$ has the shape described by (1). (b) Cross-section of the model of part (a) in the plane of a meridian. The model comprises a shell V_1 (viscosity $\eta_1 \equiv \gamma\eta_2$), an upper mantle V_2 (viscosity η_2), and a lower mantle V_3 (viscosity $\eta_3 \equiv \lambda\eta_2$) bounded below by an inviscid core. The surfaces S_1, S_2 and S_3 are labeled together with their unit normals $\boldsymbol{n}$. The additional geometrical parameters h, d, θ_t, θ_s and φ_s of the model are as in fig. 1.

The required boundary-integral equations are derived in the Supporting Information. In dimensionless form, they are

$$\boldsymbol{U}_1 - (1-\gamma)\int_{S_1}(\boldsymbol{U}-\boldsymbol{U}_1)\cdot\boldsymbol{T}(\boldsymbol{x}_1)\cdot\boldsymbol{n}\mathrm{d}S + \lambda\int_{S_2}\boldsymbol{U}\cdot\boldsymbol{T}(\boldsymbol{x}_1)\cdot\boldsymbol{n}\mathrm{d}S - (1-\lambda)\int_{S_3}\boldsymbol{U}\cdot\boldsymbol{T}(\boldsymbol{x}_1)\cdot\boldsymbol{n}\mathrm{d}S = -\int_{S_1}(r-r_1)\boldsymbol{n}\cdot\boldsymbol{G}(\boldsymbol{x}_1)\mathrm{d}S + (\alpha_2-\alpha_3)\int_{S_2}(r-R_2)\boldsymbol{n}\cdot\boldsymbol{G}(\boldsymbol{x}_1)\mathrm{d}S - \alpha_3\int_{S_3}(r-R_3)\boldsymbol{n}\cdot\boldsymbol{G}(\boldsymbol{x}_1)\mathrm{d}S, \quad (27a)$$

$$\lambda\boldsymbol{U}_2 - (1-\gamma)\int_{S_1}\boldsymbol{U}\cdot\boldsymbol{T}(\boldsymbol{x}_2)\cdot\boldsymbol{n}\mathrm{d}S + \lambda\int_{S_2}(\boldsymbol{U}-\boldsymbol{U}_2)\cdot\boldsymbol{T}(\boldsymbol{x}_2)\cdot\boldsymbol{n}\mathrm{d}S - (1-\lambda)\int_{S_3}\boldsymbol{U}\cdot\boldsymbol{T}(\boldsymbol{x}_2)\cdot\boldsymbol{n}\mathrm{d}S = -\int_{S_1}r\boldsymbol{n}\cdot\boldsymbol{G}(\boldsymbol{x}_2)\mathrm{d}S + (\alpha_2-\alpha_3)\int_{S_2}(r-R_2)\boldsymbol{n}\cdot\boldsymbol{G}(\boldsymbol{x}_2)\mathrm{d}S - \alpha_3\int_{S_3}(r-R_3)\boldsymbol{n}\cdot\boldsymbol{G}(\boldsymbol{x}_2)\mathrm{d}S, \quad (27b)$$

$$\boldsymbol{U}_3 - (1-\gamma)\int_{S_1}\boldsymbol{U}\cdot\boldsymbol{T}(\boldsymbol{x}_3)\cdot\boldsymbol{n}\mathrm{d}S + \lambda\int_{S_2}\boldsymbol{U}\cdot\boldsymbol{T}(\boldsymbol{x}_3)\cdot\boldsymbol{n}\mathrm{d}S - (1-\lambda)\int_{S_3}(\boldsymbol{U}-\boldsymbol{U}_3)\cdot\boldsymbol{T}(\boldsymbol{x}_3)\cdot\boldsymbol{n}\mathrm{d}S = -\int_{S_1}r\boldsymbol{n}\cdot\boldsymbol{G}(\boldsymbol{x}_3)\mathrm{d}S + (\alpha_2-\alpha_3)\int_{S_2}(r-R_2)\boldsymbol{n}\cdot\boldsymbol{G}(\boldsymbol{x}_3)\mathrm{d}S - \alpha_3\int_{S_3}(r-R_3)\boldsymbol{n}\cdot\boldsymbol{G}(\boldsymbol{x}_3)\mathrm{d}S, \quad (27c)$$

where $\alpha_2 = \delta\rho_2/\delta\rho_1$ and $\alpha_3 = \delta\rho_3/\delta\rho_1$. In (27), all lengths (including R_2 and R_3) have been nondimensionalized by R_0 and all velocities by $g\delta\rho_1 R_0^2/\eta_2$. $\boldsymbol{G}$ and $\boldsymbol{T}$ are Green's functions for the velocity and stress, respectively, at the point $\boldsymbol{x}_m$ ($m = 1$, 2 or 3) generated by a point force acting at $\boldsymbol{x}$ (the variable of integration). The equations (27) are three coupled Fredholm integral equations of the second kind for the velocities $\boldsymbol{U}_1$, $\boldsymbol{U}_2$ and $\boldsymbol{U}_3$ on the surfaces S_1, S_2 and S_3, respectively. The points $\boldsymbol{x}_1$, $\boldsymbol{x}_2$ and $\boldsymbol{x}_3$ are arbitrary field or observation points on S_1, S_2 and S_3. To simplify the notation, the argument $\boldsymbol{x}$ has been everywhere suppressed. We also use the shorthand notation $r_m = r(\boldsymbol{x}_m)$ and $\boldsymbol{U}_m = \boldsymbol{U}(\boldsymbol{x}_m)$. The Green's functions $\boldsymbol{G}(\boldsymbol{x}_m)$ and $\boldsymbol{T}(\boldsymbol{x}_m)$ are the same as those in the axisymmetric model before the azimuthal integration is performed.

The integrals on the right-hand sides of (27a)–(27c) are called single-layer integrals, and represent the driving force of buoyancy. The integrals on the left-hand sides are called double-layer integrals, and are required to ensure the matching of velocity and stress across interfaces between fluids with different viscosities. An explanation of how (27) are solved is given in the Supporting Information (Dziewonski & Anderson, 1981; Pozrikidis, 1992; Hackbusch, 1999; Pozrikidis, 2002; Chaillat et al., 2017).

Figures 2e–h show several diagnostic properties of a BEM solution for a 3-D model with $\phi_f = 90°$ but without viscosity stratification or an inviscid core. All properties are shown as functions of arclength s along the mirror plane $\phi = 0$ of the shell, and can be compared directly with the corresponding properties for an axisymmetric shell shown in figures 2a–d. Figures 2a and 2e show that the presence of the free edge in the 3-D case allows the plate to translate as a whole. Subduction is therefore no longer due entirely to trench rollback as it was in the axisymmetric case. However, this difference is not accompanied by a corresponding difference in the flexural dynamics. The profiles of the radial velocity u_r (figs. 2b and 2f) and the bending rate $\dot{B}_\theta$ (figs. 2c and 2g) are nearly indistinguishable between the 3-D and axisymmetric cases for $s/R_0 > 0.3$. However, for $s/R_0 < 0.17$ both u_r and $\dot{B}_\theta$ are nonzero in the 3-D case, due to the slow downward flexure of the free edge.

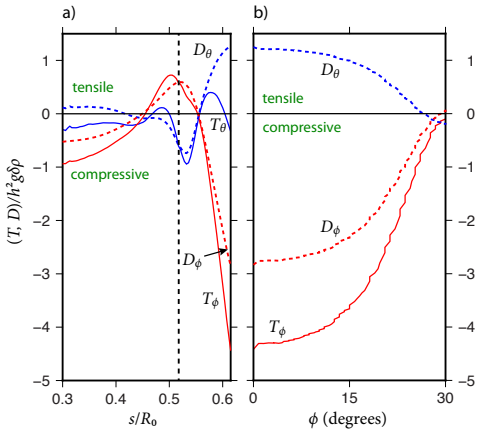

Figure 7. Stress resultants for a 3-D convex shell with the standard parameters of Table 1 and $\phi_f = 30°$. (a) Stress resultants versus arclength along the midsurface in the mirror plane $\phi = 0$. The black dashed line shows the position of the trench. (b) Resultants as functions of longitude along the leading edge $\theta = \theta_s$ of the slab. T_θ is not shown because it is close to zero on the free leading edge.

In fig. 2h, the flexural dissipation is not shown and the membrane dissipation is shown only for $s/R_0 > 0.14$. This is due to numerical instability in the calculation of the kinematical quantities $\dot{\kappa}_\phi$ and $\dot{\epsilon}_\phi$, which are small differences of much larger numbers. Comparing figs. 2d and 2h, we see that the membrane dissipation rate in the slab is similar in the two cases. However, in the plate interior $s/R_0 < 0.54$ the dissipation rate is about ten times larger in the 3-D case. This dissipation is associated with shortening, not extension.

Fig. 7a shows the stress resultants T_θ, T_ϕ, D_θ, and D_ϕ in the mirror plane $\phi = 0$ for the standard parameters of Table 1 and $\phi_f = 30°$. The stress resultants are still defined by (21) and (23), but with $\dot{\epsilon}_\theta$ and $\dot{\epsilon}_\phi$ given by (A2). The curves are very similar to those for the axisymmetric case (fig. 5b), and the deviatoric hoop stress dominates in the slab with $D_\phi \approx -2D_\theta$.

Fig. 7b shows how the resultants vary with longitude on the leading end $\theta = \theta_s$ of the slab. The (compressive) deviatoric hoop stress is still dominant with $D_\phi \approx -2D_\theta$, where D_θ is the (tensile) deviatoric downdip stress resultant. The resultants are roughly constant for $\phi < 10°$ and then tend to zero at $\phi = 30°$, which corresponds to the (stress-free) corner of the slab.

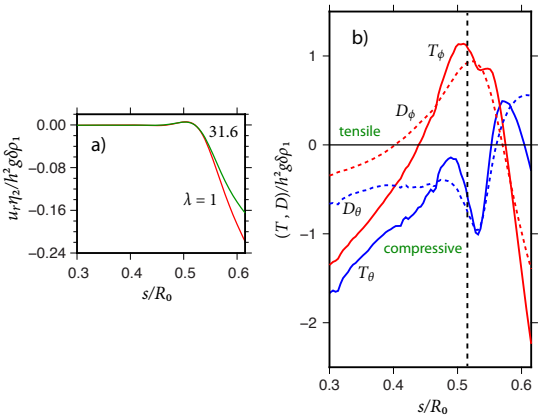

Figure 8. Effect of mantle viscosity stratification on the subduction rate and the stress state in the slab, for the shell shown in fig. 6a and with the standard parameters of Table 1. (a) radial velocity $u_r(s)$ of the midsurface in the mirror plane $\phi = 0$ for $\lambda = 31.6$ and $\lambda = 1$. (b) stress resultants $T_\theta(s)$, $T_\phi(s)$, $D_\theta(s)$, and $D_\phi(s)$ in the mirror plane for $\lambda = 31.6$. The black dashed line shows the position of the trench. The corresponding curves for $\lambda = 1$ are those of fig. 7a.

5 Effect of viscosity stratification

As a step towards greater geophysical realism, we now examine a new model (fig. 6b) in which the viscosity of the lower mantle exceeds that of the upper mantle by a factor $\lambda = 10^{1.5} = 31.6$, identical within uncertainty to the standard value of 30 inferred from internal loading models (Hager et al., 1985). To isolate the effect of this viscosity jump we continue to ignore the presence of the core.

The boundary-integral equations for the new model are obtained from (27) by ignoring (27b) and eliminating the integrals over S_2 from (27a) and (27c). We also suppose that S_3 is perfectly spherical, so that the single-layer integrals over S_3 vanish.

Fig. 8a shows the radial velocity $u_r(s)$ on the mirror plane $\phi = 0$ of the shell shown in fig. 6a, for both $\lambda = 31.6$ and $\lambda = 1$. $|u_r|$ is smaller in the former case, indicating that the stiffer upper surface of a high-viscosity lower mantle reduces the rate of subduction. Fig. 8b shows the corresponding stress resultants for $\lambda = 31.6$. The state of deviatoric stress is dominated by the hoop stress in the lower part of the slab, where $D_\phi \approx -2D_\theta$. In the upper part, however, the hoop and downdip stresses are comparable ($D_\phi \approx -D_\theta$). The corresponding resultants for an isoviscous mantle ($\lambda = 1$) are shown in fig. 7a.

We close this section with a few words about the influence of an inviscid core. For reasons explained in the Supporting Information, we estimated the influence of the core

using an alternative model in which flow is driven by the imposed radial deformation of a thin, highly viscous spherical shell in the mid upper mantle (Supporting Information, Figure S1). We find that the effect of the core on the radial velocity of the thin layer is at most 7% for spherical harmonic degree $l = 2$, and negligible for degrees $l \approx 50$–100 characteristic of subducted slabs. We conclude that one can neglect the core in spherical subduction modeling, and that a more important viscosity jump to include is the one at 660 km depth.

6 Subduction zones with negative Gaussian curvature

In the models examined hitherto, the trench is convex when viewed from the landward side. Examples of such trenches are Cascadia, Central America, the eastern Aleutian, and the northern Mariana. However, many subduction zones have trenches that are totally or partly concave: examples include the western Aleutian and the southern Mariana. Concave subduction zones differ from convex ones in that their Gaussian curvature G is negative.

To understand better the dynamics of concave subduction zones, we consider the shell shown in fig. 9a. The trench is now concave landward, and is a portion of a small circle with radius 17.2°. The plate has $\phi_f = 20°$, and the shape of the slab is given by equation (1) in sections normal to the trench. The values of all other parameters are those of Table 1.

Figure 9b shows the resultants of the total and deviatoric downdip (blue) and hoop stresses (red) as a function of arclength along the midsurface in the mirror plane. Interestingly, the deviatoric stress resultants now change sign near the lower end of the slab, such that D_ϕ is compressive in the upper part of the slab and tensile in its lowermost part. Yet throughout the slab, the approximate relation $D_\phi \approx -2D_\theta$ holds, as it did for our models with a convex trench. We were unable to calculate reliably the resultants along the leading edge of the slab due to numerical instability (small differences of large numbers).

7 Testing the models: The Mariana subduction zone

We now test the predictions of our BEM models using observations in the Mariana Trench region. In this subduction zone, the slab is strongly curved in both the downdip and along-strike directions. In the simple axisymmetric model studied in § 3 , θ and ϕ are the colatitude and longitude, which naturally correspond to the down-dip and along-strike direction since the symmetry axis passes through the north pole. However, the down-dip and along-strike directions in real-world subduction zones do not in general align with geographic spherical coordinates. To minimize the introduction of new notation, we extend the meaning of the symbols θ and ϕ to the local downdip and along-strike directions, respectively, and use the symbols u and v for the longitude and latitude of the global spherical coordinate system.

Figure 10a shows a map view of the Mariana region, and fig 10b shows a 3-D view of the slab from the Slab2 dataset (Hayes et al., 2018). The slab geometry changes from convex in the north (21-26°N) to concave in the south (12-19°N). The concavity/convexity of the slab is determined by the along-strike curvature K_ϕ, which we estimate as

$$K_\phi \approx -\frac{(r_{uu}r_v^2 - 2r_u r_v r_{uv} + r_u^2 r_{vv})\cos v}{r_1(r_u^2 + r_v^2)^{3/2}} \tag{28}$$

where $r(u, v)$ is the radius of the slab surface as a function of longitude u and latitude v and subscripts u and v indicate partial differentiation. The formula (28) gives the curvature of a line defined by the implicit equation $r(u, v) = r_1$, which corresponds to the intersection of the slab surface with a sphere of radius r_1. The formula is valid when the

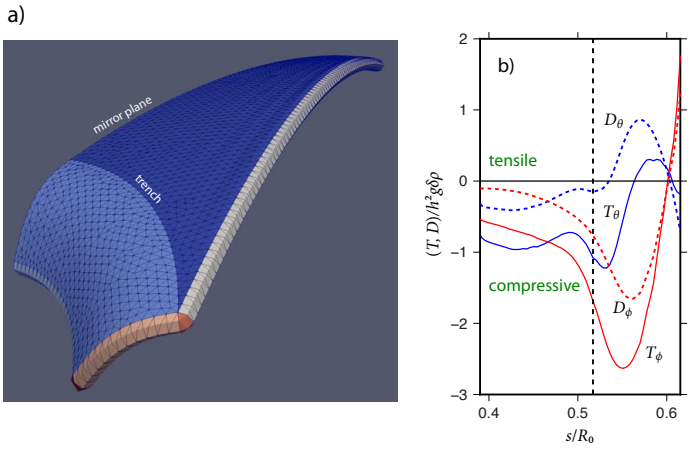

Figure 9. State of stress in a shell with a concave trench. (a) Bird's-eye view of the shell. The opening angle is $\phi_f = 20°$, and the radius of the trench is 17.2°. Other parameters are as in Table 1. (b) Downdip (blue) and hoop (red) stress resultants along the mirror plane. The black dashed line shows the position of the trench.

local curvature is much larger than $1/r_1$, which is generally the case for slabs. Since the tangent to the curve $r(u, v) = r_1$ defines the strike direction, we refer to K_ϕ as the along-strike curvature. The calculated values of K_ϕ are shown by blue and red in fig. 10a, projected onto the surface from their different depths (increasing from east to west). Figure 10a also shows earthquake focal mechanisms (beachball diagrams) which we use to estimate the local state of stress. For a double-couple moment solution (not to be confused with a bending moment), the T-axis (red sector of the beach ball) and the P-axis (white sector) correspond to the tensile and compressive directions, respectively.

In general, there are four possible combinations of slab geometry and the sign of the hoop stress: convex/compressive, concave/compressive, concave/tensile, and convex/tensile. Our BEM models predict that concave-landward slabs can exhibit both compressive and tensile hoop stress depending on the depth, whereas the hoop stress in convex slabs is always compressive. To test this prediction, we estimate the stress state in the Mariana slab using focal mechanisms from all earthquakes with magnitudes > Mw5 from the GCMT catalogue (Ekstrom et al., 2012) that are located within 100 km of the Mariana subduction zone interface given by Slab2 (fig. 10b). For each earthquake, we estimate the dimensionless deviatoric stress $\boldsymbol{\tau}$ as

$$\boldsymbol{\tau} = M_0^{-1}\left(\boldsymbol{M} - \frac{1}{3}(\mathrm{tr}\boldsymbol{M})\boldsymbol{I}\right) \tag{29}$$

where $\boldsymbol{M}$ is the moment tensor, and M_0 is the moment magnitude, and $\boldsymbol{I}$ is the identity tensor. The hoop stress is then $\tau_{\phi\phi} = \boldsymbol{e}_\phi \cdot \boldsymbol{\tau} \cdot \boldsymbol{e}_\phi$ where $\boldsymbol{e}_\phi$ is the along-strike direction. For each earthquake, we calculate the along-strike curvature at the point on the slab interface that is closest to the event.

Figure 11a shows a plot of $\tau_{\phi\phi}$ vs. K_ϕ for the earthquakes in the northern (blue) and southern (red) portions of the Mariana slab. The slab geometry and sign of the hoop stress for each quadrant of the diagram are indicated in green. The NE, SE, and SW quadrants are heavily populated with earthquakes, but the NW (convex/tensile) quadrant is almost empty, validating the prediction of our BEM models.

Another prediction of our BEM models is that the magnitude of the deviatoric hoop stress in slabs significantly exceeds that of the downdip stress. To test this prediction, we show in figure 11b the hoop stress $\tau_{\phi\phi}$ vs. the downdip stress $\tau_{\theta\theta}$ for all the Mariana earthquakes in our catalog. The hoop stress is dominant in quadrants I and III, whereas the downdip stress is dominant in quadrants II and IV. Earthquakes with dominant hoop stress and those with dominant downdip stress are roughly equal in number, supporting partially (but only partially) the prediction of the BEM models.

8 Discussion

The first notable result of this study is the importance of distinguishing between geometrical and dynamical effects of sphericity on subduction dynamics. The former is greater for a larger shell, whose midsurface differs more from a plane than that of a small one. This purely geometrical effect can be characterized by a geometrical sphericity number

$$\Sigma_G = \theta_t \tag{30}$$

which is simply the angular radius of the trench (or the minimum radius if the trench is concave). However, the dynamical sphericity effect has the opposite trend: it is greater for a small plate than for a large one. This is so because the dynamical effect of sphericity is measured by the dynamical sphericity number

$$\Sigma_D = \frac{l_b}{R_0}\cot\theta_t \tag{31}$$

which for a given l_b is greater for a smaller plate.

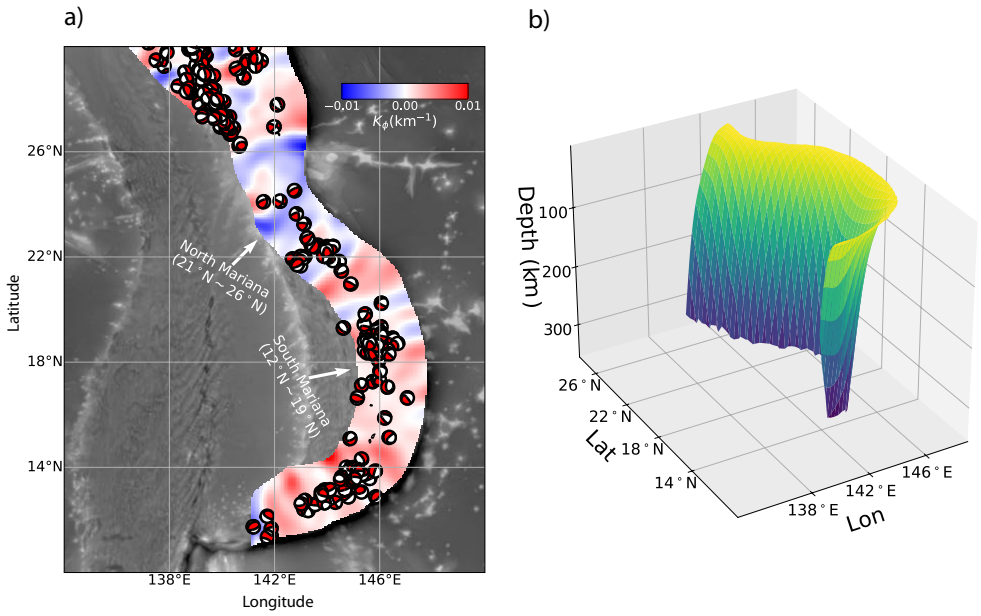

Figure 10. a) Map view of the Mariana subduction zone. Along-strike curvature K_ϕ derived from Slab2 (Hayes et al., 2018) is color-coded. Beachballs show focal mechanisms of earthquakes larger than Mw5.5 from the GCMT catalogue (Ekstrom et al., 2012). b) Mariana slab geometry from Slab2 from the surface to 300 km depth. The lateral scales are stretched by a factor of 4 relative to the vertical scale.

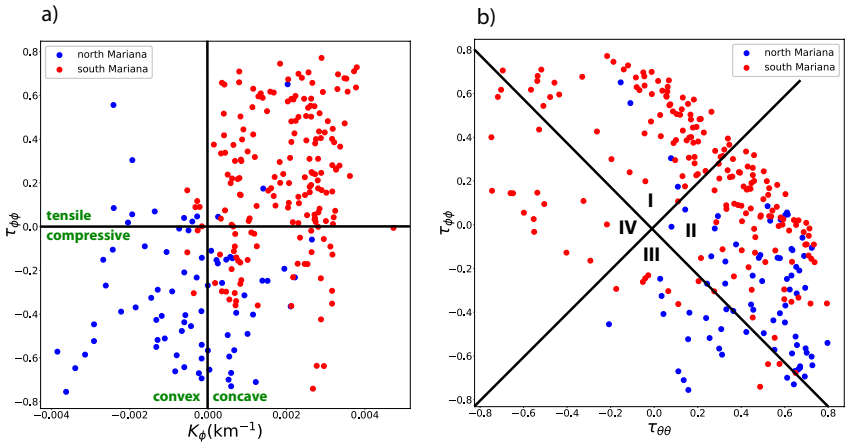

Figure 11. Distributions of stress and curvature in the northern (blue) and southern (red) Mariana subduction zone, determined as described in the text. a) Dimensionless deviatoric hoop stress $\tau_{\phi\phi}$ vs. along-strike curvature K_ϕ. Portions of the figure corresponding to convex vs. concave geometry and tensile vs. compressive stress are indicated. b) $\tau_{\phi\phi}$ vs. dimensionless down-dip stress $\tau_{\theta\theta}$. Hoop stress is dominant in quadrants I and III, and downdip stress in quadrants II and IV.

Under what conditions is dynamical sphericity negligible? This question can be answered by writing the definition (31) in an alternative way as $\Sigma_D = (l_b/L)\epsilon\cot\epsilon$ where $\epsilon = L/R_0$ and L is the plate radius measured along the Earth's surface. The limit of negligible sphericity $\Sigma_D \to 0$ then occurs either when $\epsilon = \pi/2$ (a hemispherical shell) or when $l_b/L \to 0$ for arbitrary ϵ. Both of these limiting cases imply that the dynamical sphericity effect is smaller for larger shells. As an extreme example, consider the Earth's largest plate, the Pacific plate. Modelling this plate crudely as a spherical cap of area $A = 1.05 \times 10^8$ km^2 (Bird, 2003), we find $L = 6000$ km and $\epsilon = 0.94$. Then for a representative bending length $l_b \approx 900$ km, we find $\Sigma_D \approx 0.1$, a very small value. Dynamical sphericity is therefore unlikely to be important for the Pacific plate, although it will be much more important for smaller plates.

Our BEM models predict that not all combinations of the signs of the along-strike curvature (convex or concave) and of the hoop stress (compressive or tensile) can exist in subducted slabs. We find that concave-landward slabs can exhibit both compressive and tensile hoop stress depending on the depth, whereas the hoop stress in convex slabs is always compressive. We tested this prediction using slab geometry and earthquake focal mechanism data from the Mariana subduction zone to locate the earthquakes on a plot of dimensionless hoop stress vs. along-strike curvature. As expected, the concave/compressive, concave/tensile and convex/compressive quadrants of the diagram are densely populated with earthquakes, while the convex/tensile quadrant is almost empty (fig. 11a).

Another prediction of our models is that the state of deviatoric stress in slabs is dominated by the hoop stress. For a wide range of models, we find the 'rule of thumb' $D_\phi \approx -2D_\theta$, where D_ϕ and D_θ are the resultants of the deviatoric hoop stress and downdip stress, respectively. This rule is a direct consequence of the definitions (23) when $|T_\phi| \gg |T_\theta|$. Note that D_ϕ and D_θ nearly always have opposite signs. The importance of hoop stresses is a consequence of the doubly-curved character of spherical shells, and has no analog in singly-curved shells with zero Gaussian curvature.

However, our prediction of dominant hoop stress is only partially supported by centroid moment tensor data from the Mariana subduction zone. Figure 11b shows that there are indeed many earthquakes with dominant hoop stresses (quadrants I and III), but that the earthquakes with dominant downdip stress (quadrants II and IV) are at least as numerous.

A possible explanation for the lack of a consistent relation between $\tau_{\phi\phi}$ and $\tau_{\theta\theta}$ is that Mariana earthquakes occur at different distances z from the slab's neutral surface where the midsurface-parallel normal stress changes sign. Equations (9.7) and (4.25) of Novozhilov (1959) show that the (total) normal stresses within a deforming shell are

$$\sigma_{\theta\theta} = 4\eta_1 \left[\dot\epsilon_\theta + \frac{1}{2}\dot\epsilon_\phi + z\left(\dot K_\theta + \frac{1}{2}\dot K_\phi\right)\right], \tag{32a}$$

$$\sigma_{\phi\phi} = 4\eta_1 \left[\dot\epsilon_\phi + \frac{1}{2}\dot\epsilon_\theta + z\left(\dot K_\phi + \frac{1}{2}\dot K_\theta\right)\right]. \tag{32b}$$

where z is the coordinate normal to the midsurface $z = 0$. Here $\dot K_\theta = \dot\kappa_\theta + K_\theta\dot\epsilon_\theta$ and $\dot K_\phi = \dot\kappa_\phi + K_\phi\dot\epsilon_\phi$ are the rates of change with time of the curvatures of the midsurface in the downdip and along-strike directions, respectively, associated with deformation by bending. Earthquakes occurring at different values of z will therefore 'feel' different amounts of bending stress, leading to a complex relationship between $\sigma_{\phi\phi}$ and $\sigma_{\theta\theta}$.

In most of our 3-D models the stress in the interior of the plate is compressive. This result is also predicted by the 2-D BEM solutions of Ribe (2010), for which the plate is flat in its undeformed state. The origin of intraplate compressive stress can be understood using a simple 1-D model for the deformation of a thin viscous plate moving in the x-direction with speed $U(x)$. The flow within the plate satisfies $4\eta_1 hU'' + \sigma_{xz} =$

0, where primes denote derivatives and σ_{xz} is the shear stress acting on the base of the plate. Integrating once and applying the boundary condition $U'(0) = U'_0$, we find

$$4\eta_1 h U' = 4\eta_1 h U'_0 - \int_0^x \sigma_{xz} \mathrm{d}x \equiv N_0 - \int_0^x \sigma_{xz} \mathrm{d}x \tag{33}$$

where N_0 is the force (per unit length 'into the page') applied to the trailing end of the plate. The solution (33) shows that the intraplate stress is compressive ($U' < 0$) if $N_0 < 0$ and $\sigma_{xz} > 0$, signs that correspond to forces that push the plate in the direction of its motion. These forces are generated by the large-scale cellular flow driven by the subducting slab, wherein streamlines originating on the slab reconnect to the plate's trailing edge and lead to a non-trivial ambient dynamic pressure around the plate (Goldberg & Holt, 2024).

The large compressive hoop stress in our models with both convex and concave trenches can in principle drive longitudinal buckling instabilities with fold axes parallel to the downdip direction (Scholz & Page, 1970; Bayly, 1982). Such buckling, if it occurs, can have a major effect on the behavior of the slab in the mantle transition zone (MTZ). Theoretical (Ribe et al., 2007) and numerical (Lee & King, 2011; Cížková & Bina, 2013) studies suggest that slabs encountering an increase of viscosity at 660 km depth can buckle periodically, creating piles of folds whose axes are horizontal. If however longitudinal buckling at shallower depths has corrugated the slab and thereby stiffened it, periodic folding will be more difficult. Exploring the interaction between longitudinal buckling and horizontal periodic folding is beyond the scope of the present study, but will be the subject of future work.

We close with a few words on the relevance of hoop stresses to the focal mechanisms of deep earthquakes. Even though the Mariana CMT data suggest that the hoop stress is not always dominant in subducting slabs, it nevertheless exceeds the down-dip stress for about half the earthquakes we examined. The hoop stress may therefore play an important role as a driving mechanism of deep earthquakes. It has already been suggested that downdip stresses associated with the bending and unbending of subducted slabs may generate deep intraplate earthquakes and double Wadati-Benioff zones (Sandiford et al., 2019; Sippl et al., 2022). Our boundary-element models and our statistical analysis of Mariana earthquakes suggest that hoop stresses associated with the lateral stretching and compression of the subducted slab may be an equally important mechanism for generating deep earthquakes. We leave for future work the extension of our analysis to other subduction zones in the Pacific ocean and elsewhere.

Appendix A Kinematical quantities and dissipation rates

The rate of deformation of the midsurface of a thin viscous shell is described by six kinematical quantities. The rate of membrane deformation is described by two rates of extension $\dot{\epsilon}_\theta$ and $\dot{\epsilon}_\phi$ and a rate of shear ω. The rate of flexural deformation is described by two rates of bending $\dot{\kappa}_\theta$ and $\dot{\kappa}_\phi$ and a rate of twisting τ. The general expressions for these quantities in terms of the components (U, V, W) of the midsurface velocity and their derivatives are given by eqns. (4.23) of Novozhilov (1959), and are

$$\dot{\epsilon}_\theta = B_\theta \partial_\theta U + B_\theta B_\phi \partial_\phi A_\theta V - K_\theta W, \tag{A1a}$$

$$\dot{\epsilon}_\phi = B_\phi \partial_\phi V + B_\theta B_\phi \partial_\theta A_\phi U - K_\phi W, \tag{A1b}$$

$$\omega = A_\phi B_\theta \partial_\theta \left(B_\phi V\right) + A_\theta B_\phi \partial_\phi \left(B_\theta U\right), \tag{A1c}$$

$$\dot{\kappa}_\theta = -B_\theta \partial_\theta \left(B_\theta \partial_\theta W + K_\theta U\right) - B_\theta B_\phi \partial_\phi A_\theta \left(B_\phi \partial_\phi W + K_\phi V\right), \tag{A1d}$$

$$\dot{\kappa}_\phi = -B_\phi \partial_\phi \left(B_\phi \partial_\phi W + K_\phi V\right) - B_\theta B_\phi \partial_\theta A_\phi \left(B_\theta \partial_\theta W + K_\theta U\right), \tag{A1e}$$

$$\tau = -B_\theta B_\phi \partial^2_{\theta\phi} W + B_\theta^2 B_\phi \partial_\phi A_\theta \partial_\theta W - K_\theta (B_\phi \partial_\phi U - B_\theta B_\phi \partial_\phi A_\theta U) + B_\theta B_\phi^2 \partial_\theta A_\phi \partial_\phi W - K_\phi (B_\theta \partial_\theta V - B_\theta B_\phi \partial_\theta A_\phi V). \quad \text{(A1f)}$$

where $B_\theta = 1/A_\theta$ and $B_\phi = 1/A_\phi$.

In our models with a convex trench the cross-sectional shape of the shell is independent of ϕ, which implies $\partial_\phi A_\theta = \partial_\phi A_\phi = \partial_\phi K_\theta = \partial_\phi K_\phi = 0$. Equations (A1) then take the simpler forms

$$\dot\epsilon_\theta = B_\theta \partial_\theta U - K_\theta W, \quad \text{(A2a)}$$

$$\dot\epsilon_\phi = B_\phi \partial_\phi V + B_\theta B_\phi \partial_\theta A_\phi U - K_\phi W, \quad \text{(A2b)}$$

$$\omega = A_\phi B_\theta \partial_\theta \left(B_\phi V\right) + B_\phi \partial_\phi U, \quad \text{(A2c)}$$

$$\dot\kappa_\theta = -B_\theta \partial_\theta \left(B_\theta \partial_\theta W + K_\theta U\right), \quad \text{(A2d)}$$

$$\dot\kappa_\phi = -B_\phi (B_\phi \partial^2_{\phi\phi} W + K_\phi \partial_\phi V) - B_\theta B_\phi \partial_\theta A_\phi \left(B_\theta \partial_\theta W + K_\theta U\right), \quad \text{(A2e)}$$

$$\tau = -B_\theta B_\phi \partial^2_{\theta\phi} W - K_\theta B_\phi \partial_\phi U + B_\theta B_\phi^2 \partial_\theta A_\phi \partial_\phi W - K_\phi (B_\theta \partial_\theta V - B_\theta B_\phi \partial_\theta A_\phi V). \quad \text{(A2f)}$$

In some cases our calculations of the kinematical quantities are limited to the mirror plane $\phi = 0$, where $V = \partial_\phi U = \partial_\phi W = 0$. The quantities ω and τ then vanish identically, while $\dot\epsilon_\theta$, $\dot\epsilon_\phi$, $\dot\kappa_\theta$, and $\dot\kappa_\phi$ retain their forms (A2). The final simplification is for the axisymmetric deformation of an axisymmetric shell, for which (A2) simplify to

$$\dot\epsilon_\theta = B_\theta \partial_\theta U - K_\theta W, \quad \text{(A3a)}$$

$$\dot\epsilon_\phi = B_\theta B_\phi \partial_\theta A_\phi U - K_\phi W, \quad \text{(A3b)}$$

$$\omega = 0, \quad \text{(A3c)}$$

$$\dot\kappa_\theta = -B_\theta \partial_\theta \left(B_\theta \partial_\theta W + K_\theta U\right), \quad \text{(A3d)}$$

$$\dot\kappa_\phi = -B_\theta B_\phi \partial_\theta A_\phi \left(B_\theta \partial_\theta W + K_\theta U\right), \quad \text{(A3e)}$$

$$\tau = 0. \quad \text{(A3f)}$$

The rates of viscous dissipation Φ per unit midsurface area associated with membrane and flexural deformation can be calculated from the quantities defined above. The membrane and flexural energies per unit midsurface area of a deformed elastic shell are the quantities in square brackets in (9.12) of Novozhilov (1959). Transforming these to expressions for dissipation rates in a viscous shell using the Stokes-Rayleigh analogy (Ribe, 2018), we obtain

$$\Phi_m = 2\eta_1 h \left[\dot\epsilon_\theta^2 + \dot\epsilon_\phi^2 + \dot\epsilon_\theta \dot\epsilon_\phi + \frac{\omega^2}{4}\right], \quad \Phi_f = \frac{1}{6}\eta_1 h^3 \left[\dot\kappa_\theta^2 + \dot\kappa_\phi^2 + \dot\kappa_\theta \dot\kappa_\phi + \tau^2\right], \quad \text{(A4)}$$

where m and f stand for 'membrane' and 'flexural', respectively.

Open Research

The 3-D spherical boundary-element code used in this research is available from Ribe et al. (2023).

Acknowledgments

N.M.R. was supported by the Progamme National de Planétologie (PNP) of the Institut des Sciences de l'Univers (INSU) of the CNRS, co-funded by CNES. Y. L. was supported by the ERC Advanced Grant SOFT-PLANET (PI Anne Davaille). We thank R. Katz, G. Morra and an anonymous referee for thorough and constructive reviews that helped greatly to improve the original manuscript. We also thank L. Le Pourhiet for helpful suggestions.

References

Audoly, B., & Pomeau, Y. (2010). *Elasticity and Geometry: From Hair Curls to the Non-Linear Response of Shells*. Oxford University Press.

Balázs, A., Faccenna, C., Ueda, K., Funiciello, F., Boutoux, A., Blanc, E., & Gerya, T. (2021). Oblique subduction and mantle flow control on upper plate deformation: 3d geodynamic modeling. *Earth Planet Sci. Lett.*, *569*, 117056.

Bayly, B. (1982). Geometry of subducted plates and island arcs viewed as a buckling problem. *Geology*, *10*, 629-632.

Bessat, A., Duretz, T., Hetenyi, G., Pilet, S., & Schmalholz, S. M. (2020). Stress and deformation mechanisms at a subduction zone: Insights from 2-D thermomechanical numerical modelling. *Geophys. J. Int.*, *221*, 1605-1625.

Bird, P. (2003). An updated digital model of plate boundaries. *Geochem. Geophys. Geosyst.*, *4*, doi: 10.1029/2001GC000252.

Capitanio, F. A., & Morra, G. (2012). The bending mechanics in a dynamic subduction system: Constraints from numerical modelling and global compilation analysis. *Tectonophys.*, *522-523*, 224-234.

Chaillat, S., Desiderio, L., & Ciarlet, P. (2017). Theory and implementation of H-matrix based iterative and direct solvers for Helmholtz and elastodynamic oscillatory kernels. *J. Comp. Phys.*, *351*, 165-186.

Chamolly, A., & Ribe, N. M. (2021). Fluid mechanics of free subduction on a sphere. Part 1. The axisymmetric case. *J. Fluid Mech.*, *929*, A22.

Chen, F., Davies, D. R., Goes, S., Suchoy, L., & Kramer, S. C. (2022a). Comparing the dynamics of free subduction in Cartesian and spherical domains. *Geochem. Geophys. Geosyst.*, *23*, e2022GC010757.

Chen, F., Davies, D. R., Goes, S., Suchoy, L., & Kramer, S. C. (2022b). How slab age and width combine to dictate the dynamics and evolution of subduction systems: A 3-d spherical study. *Geochem. Geophys. Geosyst.*, *23*, e2022GC010597.

Chertova, M. V., Spakman, W., & Steinberger, B. (2018). Mantle flow influence on subduction evolution. *Earth Planet. Sci. Lett.*, *489*, 258-266.

Cížková, H., & Bina, C. R. (2013). Effects of mantle and subduction-interface rheologies on slab stagnation and trench rollback. *Earth Planet. Sci. Lett.*, *379*, 95-103.

Dziewonski, A. M., & Anderson, D. L. (1981). Preliminary reference earth model. *Phys. Earth Planet. Int.*, *25*, 297-356.

Ekstrom, G., Nettles, M., & Dziewoński, A. (2012). The global CMT project 2004–2010: Centroid-moment tensors for 13,017 earthquakes. *Phys. Earth Planet. Int.*, *200-201*, 1-9.

Frank, F. C. (1968). Curvature of island arcs. *Nature*, *220*, 363.

Garel, F., Goes, S., Davies, D. R., Davies, J. H., Kramer, S. C., & Wilson, C. R. (2014). Interaction of subducted slabs with the mantle transition-zone: A regime diagram from 2-D thermo-mechanical models with a mobile trench and an overriding plate. *Geochem. Geophys. Geosyst.*, *15*, 1739-1765.

Gerya, T. (2022). Numerical modeling of subduction: State of the art and future directions. *Geosphere*, *18*, 503-561.

Goldberg, S. L., & Holt, A. F. (2024). Characterizing the complexity of subduction zone flow with an ensemble of multiscale global convection models. *Geochemistry, Geophysics, Geosystems*, *25*(2), e2023GC011134.

Hackbusch, W. (1999). A sparse matrix arithmetic based on H-matrices. Part i: Introduction to H-matrices. *Computing*, *62*, 89-108.

Hager, B. H., Clayton, R. W., Richards, M. A., Comer, R. P., & Dziewonski, A. M. (1985). Lower mantle heterogeneity, dynamic topography and the geoid. *Nature*, *313*, 541-545.

Hayes, G. P., Moore, G. L., Portner, D. E., Hearne, M., Flamme, H., Furtney, M., & Smoczyk, G. M. (2018). Slab2, a comprehensive subduction zone geometry

model. *Science*(6410), 58-61.
Laravie, J. A. (1975). Geometry and lateral strain of subducted plates in island arcs. *Geology*, *3*, 484-486.
Lee, C., & King, S. (2011). Dynamic buckling of subducting slabs reconciles geological and geophysical observations. *Earth Planet. Sci. Lett.*, *312*, 360-370.
Li, Z., & Ribe, N. M. (2012). Dynamics of free subduction from 3-D boundary element modeling. *J. Geophys. Res.*, *117*, B06408. doi: 10.1029/2012JB009165
Love, A. E. H. (1944). *The Mathematical Theory of Elasticity*. New York, New York: Dover.
Mahadevan, L., Bendick, R., & Liang, H. (2010). Why subduction zones are curved. *Tectonics*, *29*, TC6002.
Morishige, M., Honda, S., & Tackley, P. J. (2010). Construction of semi-dynamic model of subduction zoned with given plate kinematics in 3D sphere. *Earth Planets Space*, *62*, 665-673.
Morra, G., Quevedo, L., & Müller, R. D. (2012). Spherical dynamic models of top-down tectonics. *Geochem Geophys Geosyst.*, *13*, Q03005.
Morra, G., Regenauer-Lieb, K., & Giardini, D. (2006). Curvature of island arcs. *Geology*, *34*, 877-880.
Novozhilov, V. V. (1959). *The Theory of Thin Shells*. Groningen: Noordhoff.
Pozrikidis, C. (1992). *Boundary Integral and Singularity Methods for Linearized Viscous Flow*. Cambridge: Cambridge University Press.
Pozrikidis, C. (2002). *A Practical Guide to Boundary Element Methods With the Software Library BEMLIB*. Boca Raton: Chapman & Hall/CRC.
Pusok, A., Kaus, B. J. P., & Popov, A. (2018). The effect of rheological approximations in 3-D numerical simulations of subduction and collision. *Tectonophys.*, *746*, 296-311.
Ribe, N. M. (2010). Bending mechanics and mode selection in free subduction: A thin-sheet analysis. *Geophys. J. Int.*, *180*, 559-576.
Ribe, N. M. (2018). *Theoretical mantle dynamics*. Cambridge University Press.
Ribe, N. M., Chaillat, S., Li, Z.-H., Chamolly, A., & Gerardi, G. (2023). *3-D Spherical Boundary-Element Code [software]*. Retrieved from `https://doi.org/10.5281/zenodo.10019043`
Ribe, N. M., Stutzmann, E., Ren, Y., & van der Hilst, R. (2007). Buckling instabilities of subducted lithosphere beneath the transition zone. *Earth Planet. Sci. Lett.*, *254*, 173-179.
Sandiford, D., Moresi, L., Sandiford, M., & Yang, T. (2019). Geometric controls on flat slab seismicity. *Earth and Planetary Science Letters*, *527*, 115787.
Schettino, A., & Tassi, L. (2012). Trench curvature and deformation of the subducting lithosphere. *Geophys. J. Int.*, *188*, 18-34.
Scholz, C. H., & Page, R. (1970). Buckling in island arcs. *EOS (Am. Geophys. Union Trans.)*, *51*, 429.
Sippl, C., Dielforder, A., John, T., & Schmalholz, S. M. (2022). Global constraints on intermediate-depth intraslab stresses from slab geometries and mechanisms of double seismic zone earthquakes. *Geochemistry, Geophysics, Geosystems*, *23*(9), e2022GC010498.
Stegman, D., Farrington, R., Capitanio, F., & Schellart, W. (2010). A regime diagram for subduction styles from 3-D numerical models of free subduction. *Tectonophys.*, *483*, 29-45.
Tanimoto, T. (1997). Bending of a spherical lithosphere - axisymmetric case. *Geophys. J. Int.*, *129*, 305-310.
Tanimoto, T. (1998). State of stress within a bending spherical shell and its implications for subducting lithosphere. *Geophys. J. Int.*, *134*, 199-206.